Available online at www.sciencedirect.com
ScienceDirect
International Journal of Heat and Mass Transfer 51 (2008) 929–940
International Journal of HEAT and MASS TRANSFER
www.elsevier.com/locate/ijhmt

Analytical considerations of thermal radiation in cellular metal foams with open cells

C.Y. Zhao [a,c,*], S.A. Tassou [b], T.J. Lu [c]

[a] School of Engineering, University of Warwick, Coventry CV4 7AL, UK
[b] School of Engineering and Design, Brunel University, UB8 3PH, UK
[c] Xi'an Jiaotong University, Xi'an Shaanxi 710049, China

Received 27 November 2006

Abstract

An analytical model is developed to characterize the radiative transport process in highly porous, open-celled metal foams having idealized cellular morphologies in terms of fundamental radiative parameters such as emissivity, reflectivity and configuration factors. In comparison with the conventional two-flux approach or the diffusion approximation utilizing the Rosseland mean coefficient, the present model is explicit and yet relatively simple. Overall, the predicted effective radiative conductivity as a function of pore size and relative density (defined as the ratio of foam density to solid density) agrees well with that measured using a guarded-hot-plate apparatus for steel alloy foams. A systematic parametric study is subsequently carried out. The contribution of reflectance to thermal radiation is found to be significant, up to 50%, but the effect of temperature gradient is relatively small. The equivalent radiative conductivity increases linearly with increasing cell size for a fixed relative density, whilst for a given cell size the variation of relative density only has a small effect on radiation due to the mixed effects of increased emission and extinction.

Keywords: Thermal radiation; Metal foam; Modeling; Conductivity; Emission; Reflectance; Extinction; Measurement

1. Introduction

The thermal transport in highly porous, cellular metallic foams with open cells has been studied extensively in recent years [1–27]. The motivation is attributed to their high surface area to volume ratio as well as enhanced flow mixing capability due to high tortuosity. Furthermore, metallic foams have attractive mechanical properties (stiffness, strength, energy absorption etc.) [2] and sound absorption properties [12,13], and can be processed in large quantity at low cost via the metal sintering route [15]. However, the focus of most previous studies has been placed on either convective or conduction heat transfer at room or relatively low temperatures (<100 °C). Apart from low-temperature applications (e.g., compact heat exchangers for electronics cooling [1,2,15]), open-celled metal foams can also be used in high-temperature applications such as the porous radiant burner and acoustic liner in a LP (lean premixed) combustion chamber [28,29]. For such high-temperature applications, radiation in the metal foam is significant.

Zhao et al. [30] measured the effective thermal conductivity of a high temperature metal foam produced via the sintering route, FeCrAlY (Fe 73%, Cr 20%, Al 5%, Y 2%), as a function of temperature in the range of 300–800 K under both atmospheric and vacuum conditions. For FeCrAlY foams having different cell sizes and porosities, the overall effect of radiation on the whole thermal transport process (conduction, radiation and natural convection) was quantified [30]. The results show that the contribution of radiative transfer increases significantly

* Corresponding author. Address: School of Engineering, University of Warwick, Coventry CV4 7AL, UK. Tel.: +44 (0)24 7652 2339.
E-mail address: c.y.zhao@warwick.ac.uk (C.Y. Zhao).

0017-9310/$ - see front matter © 2007 Elsevier Ltd. All rights reserved.
doi:10.1016/j.ijheatmasstransfer.2007.10.010

Nomenclature

A_i	solid strut surface in unit cell, m^2	q_r	radiative heat flux, W/m^2
d	cell ligament diameter, m	Q_r	total irradiation, W
d_p	cell size, m	T	temperature, K
F	configuration factor	X, Y, Z	Cartesian coordinates
H	foam sample thickness, m	α_i	dimensionless coefficient
J	irradiation, W/m^2	β_i	dimensionless coefficient
k_c	effective thermal conductivity due to pure conduction, W/m K	ε	emissivity
		ϕ	porosity of foam
k_r	effective thermal conductivity due to pure radiation, W/m K	ρ	solid reflectance
		ρ_r	relative density
N_{cell}	total number of cells	σ	Stefan–Boltzmann constant

with increasing temperature, accounting for up to 50% of the effective (apparent) foam conductivity. Even though the contribution of natural convection can be excluded under vacuum conditions, to isolate the thermal radiation effect from the effective conductivity measurements is not straightforward. Alternatively, by using analytical models of effective foam conductivity due to solid conduction alone [5,8,10], the radiation contribution can be obtained by subtracting the conduction contribution from the measured overall conductivity in vacuum [30]. However, this is only an indirect method for studying radiation, which depends not only on the accuracy of the overall conductivity measurements but also on a reliable model of solid conduction in the metal foam.

In an attempt to acquire a better physical understanding of thermal radiation in metal foams, the spectral transmittance and reflectance of FeCrAlY foams have been measured from which their radiative properties have been obtained by Zhao et al. [31]. A numerical model based on the effective continuum medium approach is subsequently developed [31]. This model assumes that the metal foam can be approximated as a semi-transparent medium capable of absorbing, emitting and scattering radiation. Furthermore, by combining geometric optics laws with the diffraction theory, the diffusion approximation utilizing the Rosseland mean coefficient is employed. This approach can predict the spectral-dependent quantities and provide fairly good predictions in comparison with experimental measurements, and hence has the potential of being used for studying the detailed mechanisms in metal foams, including spectral absorption, extinction and scattering. However, the effective medium approach involves much complicated optical and electromagnetic theories in addition to tedious mathematical formulations, which makes the underlying physics implicit. Also, a few constants in the model must be obtained based on reliable spectral transmittance and reflectance measurements. Consequently, the effective medium approach adopted in [31] is not quite suitable for engineering applications, although it may be used to examine the spectral-dependent radiation properties in scientific research.

This study aims at establishing an explicit analytical model based on fundamental foam parameters such as emissivity, reflectance and configuration factor, and using it to establish functional relationships between the cellular structure and the radiative-transfer characteristics of open-celled metal foams. The effective medium approach will be totally abandoned, and a simple cubic cell model consisting of slender cylinders as edges will be used to capture the most important behavioral trends of radiative energy flow in the highly porous cellular foam. The predicted effective radiative conductivities will be compared with those measured in vacuum for FeCrAlY foams. It should be pointed out that the present model has been idealized in several ways to limit the complexity of radiative heat transport across an open-celled foam. Some of the simplifying assumptions made in order to analyze radiative transfer in the disordered porous material likely lead to inaccurate predictions of the actual level of heat transfer, but nevertheless should capture the approximate functional dependence of the different control variables such as foam density, cell size and temperature gradient.

2. Experimental study

A total of five FeCrAlY foam cylindrical disks of roughly 25–40 mm thickness and 100 mm diameter, with a range of pore sizes and relative densities (see Table 1), were produced via the sintering route and supplied by Porvair Fuel Cell Technology. More details of the manufacturing technique can be found in Haack et al. [15]. The typical cellular microstructure of a metal foam is shown in Fig. 1.

Table 1
The measured five samples

	Sample 1	Sample 2	Sample 3	Sample 4	Sample 5
PPI (ppi)	30	30	60	60	90
Relative density (%)	5	10	5	10	5

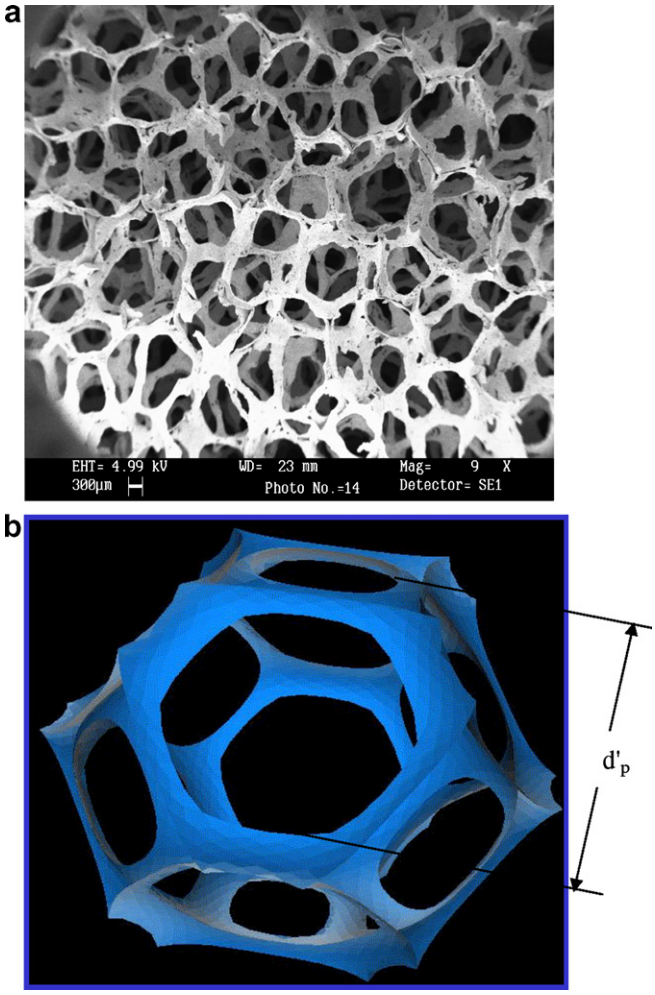

Fig. 1. Typical open-celled metal foam: (a) cellular morphology; (b) representative unit cell.

2.1. Experimental equipment

Amongst the various methods developed for thermal conductivity measurements, the guarded-hot-plate apparatus in the one-sided mode, based on ASTM C1044-90 and C177, is perhaps the most suitable and popular method. To produce a unidirectional heat flux between the top and bottom surfaces of the specimen at different temperatures and air pressures requires a complex system. The experimental apparatus consists of a test section and various support systems. The test section contains the main heater, auxiliary heaters, specimen, cooling plate, thermal insulations, and thermocouples. It is located in a vacuum chamber, which is a part of the vacuum system and enables experiments to be carried out at various air pressures. A heater control system supplies the electric power to the heaters. The cold plate temperature can be varied by adjusting the amount of air flow through the system. Thermocouple signals and power input to the main heater are recorded by a data logging system.

The specimen is placed between the electric heater (bottom surface) and the cold plate (top surface), and the heater and the cold plates are maintained at uniform temperatures, denoted here by T_h and T_c, respectively. To achieve an adiabatic condition below the heater plate, a bottom heater located beneath a layer of Microtherm® insulation material is utilized. In addition, to minimize heat loss to the sides, a side heater is placed, and the specimen and heaters are surrounded by Microtherm® insulation material. These heater arrangements and the cold plate placed on top of the specimen cause a temperature gradient in the metering region of the specimen only in the direction perpendicular to its upper and lower surfaces. Therefore the entire power input to the main heater is conducted into the specimen.

In the present measurements, the temperature difference between the cold and hot plates is roughly maintained at 40–50 K for higher temperatures and 20–30 K for lower temperatures. More details of the test apparatus design and experimental uncertainty analysis can be found in [30].

2.2. Experimental results

Under vacuum conditions the measured overall effective thermal conductivity, k_e, comprises two different modes: heat conduction and thermal radiation. For one-dimensional steady-state heat transfer across a metal foam in vacuum, the local heat flux can be approximately written as:

$$q = q_c + q_r = -(k_c + k_r)\frac{dT}{dy} = -k_e\frac{dT}{dy} \quad (1)$$

where q_c and q_r are conduction and radiation heat flux, and k_c and k_r are the corresponding equivalent conductivities due to conduction and radiation, respectively.

The analytical formulation for the conductivity k_c can be found in [6,8,10], whereas models on radiative conductivity k_r will be presented in subsequent sections based on a non-continuum approach. However, the radiative conductivity can also be obtained by subtracting the analytically predicted k_c from the measured overall thermal conductivity k_e in vacuum. The radiative conductivity thus deduced is plotted as a function of temperature in Fig. 2 for the five samples tested. The results show that the radiative conductivity increases with increasing cell size at a fixed relative density. In general, the extinction coefficient (the sum of absorption and scattering coefficients) decreases as the cell size is increased, and hence the corresponding "penetration thickness" is larger than that associated with a smaller cell size, resulting in a higher radiative conductivity as the cell size increases. More details of radiative heat transfer mechanisms will be given later.

3. Analytical model

3.1. Specifications of the model

The microstructure of a typical open-celled FeCrAlY foam consists of randomly oriented cells that are mostly homogeneous in size and shape (Fig. 1a). A single cell of

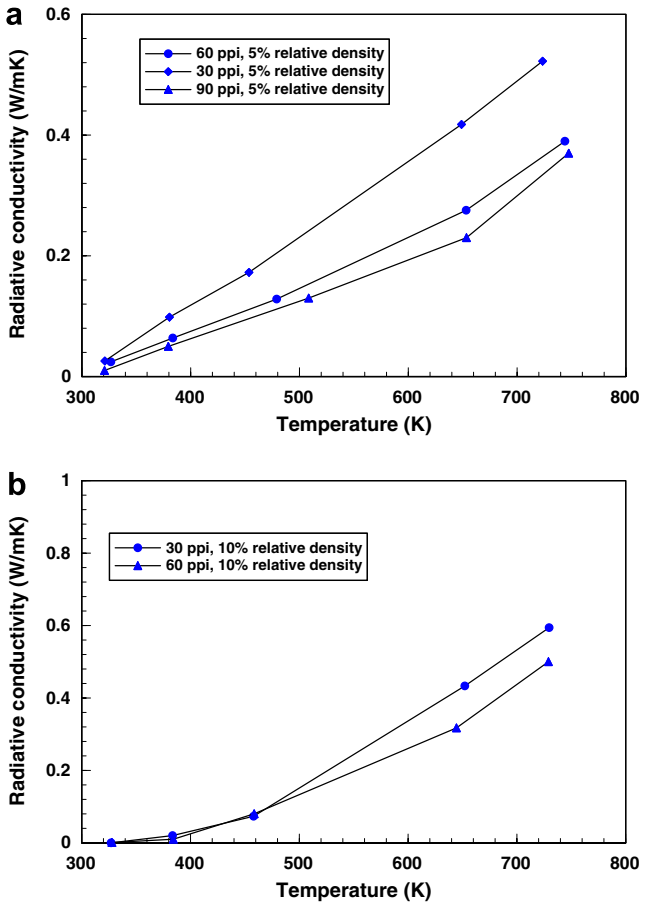

Fig. 2. Measured results for equivalent radiative conductivities: (a) 5% relative density; (b) 10% relative density.

the foam has the approximate shape of a tetrakaidecahedron with roughly 12–14 pentagonal (or hexagonal) faces of size d'_p, as shown in Fig. 1b.

With reference to Fig. 3, we consider the steady-state heat flow in an open-celled foam made up of uniform distributed, equal-sized cubic cells. The cubic unit cell is chosen for its simplicity [1,2], allowing for approximate analytical solutions for important radiative transfer parameters. The dimensions of the cell are chosen such that the surface area density of the model foam equals that of the real foam; the latter can be measured accurately by using a micro-computed-tomography system. The simple cubic unit cell shown in Fig. 3 consists of three mutually perpendicular equivalent cylinders, each having diameter d and length d_p. The relationship between d'_p and d_p based on the same porosity has been obtained [6,10], as

$$d_p \approx 0.60 d'_p \tag{2}$$

In other words, the above equation can be used to convert the pore size d'_p associated with the real foam of Fig. 1b into an equivalent cell size d_p for the idealized model of Fig. 3. The solid material (FeCrAlY) of which the metal foam is made is considered gray, and its emissivity $\varepsilon = 0.6$ is taken from the reference [32]. For FeCrAlY foams, the cell size typically varies from 0.3 mm to 3 mm or, in terms of industrial notations, from 10 ppi to 100 ppi (pores per inch).

Fig. 4 depicts the idealized foam structure, together with the conventions adopted below for analytical modeling. For simplicity, the cylinders making up the cell edges are assumed to be each parallel to the X-, Y- or Z-coordinates and referred to hereafter as cylinders X, Y and Z, respectively. With regard to the Ith unit cell (counted from the

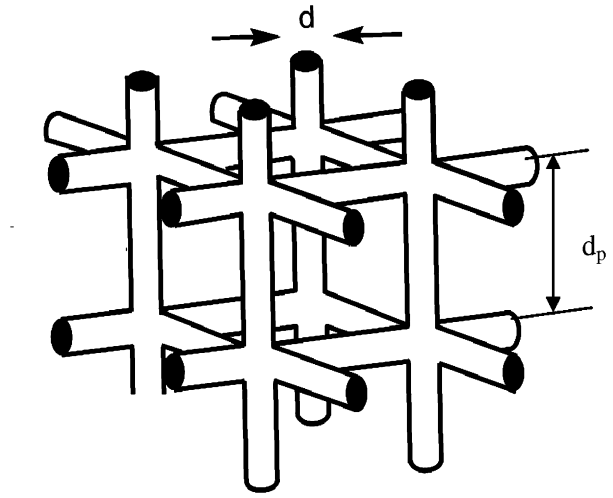

Fig. 3. Cubic unit cell.

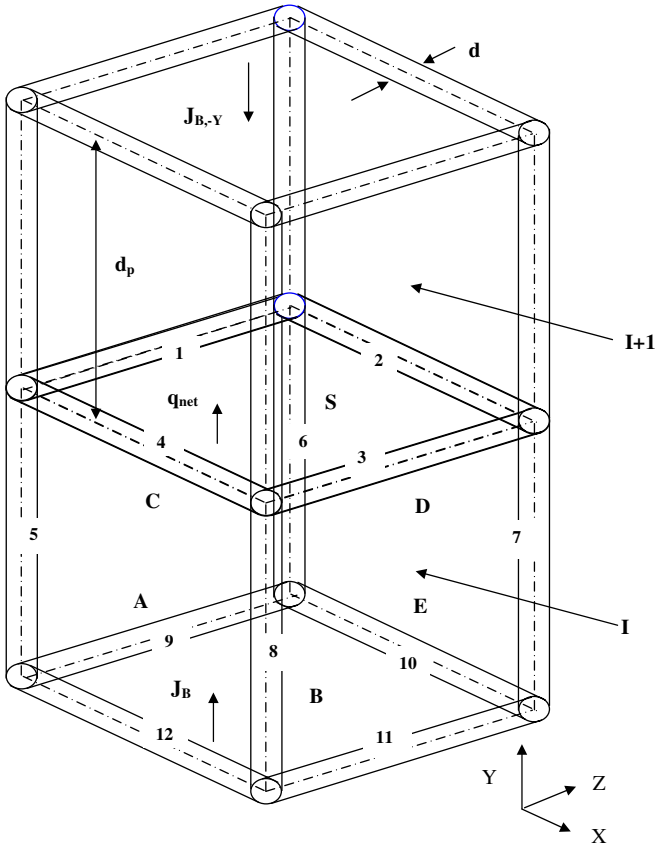

Fig. 4. Model foam structure and notations.

bottom surface of the foam sample) shown in Fig. 4, the twelve solid struts are labeled by numerical numbers 1–12, whereas the six surfaces (of the void) are designated alphabetically: the four side surfaces are referred to as A, C, D, E, whereas the top and bottom surfaces are represented by S and B, respectively. Note that only a quarter of each solid strut is included in the unit cell, the rest belonging to the neighboring cells.

In the experiment, the foams were sandwiched between two thin copper plates and the temperatures of the top and bottom surfaces were held at T_c and T_h, respectively [30]. In this analysis, without loss of generality, the condition $T_h > T_c$ is assumed such that the bulk of radiative heat flow is directed along the positive Y-direction (Fig. 4). Under vacuum conditions, the transport of heat across the metal foam comprises two competing modes – conduction and radiation. Strictly speaking, the two different transport modes are nonlinearly coupled. Due to the large porosity ($\phi \geqslant 90\%$) of the metal foam under investigation, thermal radiation emitted from the solid within a unit cell mainly passes through the void rather than striking on the solid in the neighboring cells, and the nonlinearity effect of the temperature distribution along the Y-direction is expected to be small. The model therefore assumes that radiation is decoupled from conduction and that the solid ligament temperature varies linearly with Y. The objective of the analysis is to determine the equivalent conductivity due to thermal radiation alone, namely, the radiative conductivity, k_r. As for the equivalent conductivity due to conduction alone, k_c, the three dimensional model proposed in [8] will be used.

3.2. Analysis

One-dimensional linear temperature variation in the Y-direction is assumed, and there is no temperature variation in the X- and Z-directions. Thus, on average, the temperature difference between two neighboring cells in the Y-direction is:

$$\Delta T = \frac{T_h - T_c}{N_{cell}}, \tag{3}$$

where N_{cell} is the total number of cells in the Y-direction given by:

$$N_{cell} = \frac{H}{d_p}, \tag{4}$$

and H is the thickness of the metal foam sample. The average temperature T in the Ith unit cell is

$$T = T_h - \frac{T_h - T_c}{N_{cell}} I. \tag{5}$$

For both experimental measurement [30] and the present analysis, the foam sample is sufficiently thick ($H = 25$–40 mm) such that $H \gg d_p$ is satisfied. Consequently, the small variation of temperature within the unit cell may be neglected, and the temperature T averaged over the unit cell will be used throughout the radiative analysis.

To calculate the equivalent radiative conductivity k_r, the net radiation heat flux q_{net} needs to be solved first. It is well known that the solid strut emits radiation in both positive and negative Y directions, but the radiation heat fluxes in both directions are not identical, the difference being the net radiation heat flux:

$$q_{r,net} = q_{r,Y} - q_{r,-Y} \tag{6}$$

The thermal radiation will be analyzed below based on the top void surface S of the Ith unit cell (Fig. 4).

Firstly, radiation in the positive Y-direction is examined. The total irradiation on the void surface S from the Ith unit cell includes radiation from the solid struts 5–12 and radiation from the side and bottom surfaces A–E (Fig. 4). The radiation from either the solid struts or the void surfaces comprises two contributions: emission and reflectance. The total irradiation $Q_{r,Y}$ on the top surface S can therefore be written as:

$$Q_{r,Y} = (Q_{r,Y})_{emission} + (Q_{r,Y})_{reflectance}, \tag{7a}$$

where

$$(Q_{r,Y})_{emission} = \sum_{i=5}^{12} A_i F_{iS} \cdot \varepsilon\sigma T^4 + \sum_{\Pi=A}^{E} J_\Pi F_{\Pi S} A_\Pi, \tag{7b}$$

$$\begin{aligned}(Q_{r,Y})_{reflectance} = &\sum_{i=5}^{8} (J_B F_{Bi} A_B + 2 J_A F_{Ai} A_A)\rho F_{iS} \\ &+ \sum_{i=9}^{12} (3 J_A F_{Ai} A_A)\rho F_{iS} \\ &+ \sum_{i=5}^{12} (11\varepsilon A_i F_{57}\sigma T^4)\rho F_{iS},\end{aligned} \tag{7c}$$

In the above equations, $\sigma = 5.669 \times 10^{-8}\ \mathrm{W/m^2\,K^4}$ is the Stefan–Boltzmann constant, $\rho \equiv 1 - \varepsilon$ is the solid reflectivity, $A_i = \pi d d_p/4$ is the solid surface of the ith strut ($i = 5,6,\ldots,12$) within a unit cell, J_Π and A_Π are the irradiation and surface area of the Πth surface ($\Pi = A,B,\ldots,E$), F_{iS} is the configuration factor from the ith strut to surface S, $F_{\Pi S}$ is the configuration factor from the Πth surface to surface S, whilst F_{Bi} and F_{Ai} are separately the configuration factors from bottom surface B and side surface A to the ith strut surface, with $F_{Ai} = F_{Ci} = F_{Di} = F_{Ei}$. The determination of these configuration factors will be carried out in the next section.

The first summation in Eq. (7b) represents the emission on the void surface S from the solid struts 5–12, whereas the second summation is the radiation from the side and bottom surfaces A–E, which is emitted from the solid struts of the neighboring cells. The first and second summations in Eq. (7c) represent the reflectance of the incident radiation on the solid struts 5–12 from the bottom and side surfaces of the unit cell, whilst the third summation is the reflectance of the incident radiation on the solid struts 5–12 from each other. As the configuration factors between

the slender solid struts within the unit cell are all very small and not much different, the same configuration factor F_{57} between surfaces 5 and 7 is assumed for all struts in the last summation of (7c).

Due to geometrical symmetry, the following equations hold:

$$A_5F_{5S} = A_6F_{6S} = A_7F_{7S} = A_8F_{8S}, \tag{8a}$$

$$J_AF_{AS}A_A = J_CF_{CS}A_C = J_DF_{DS}A_D = J_EF_{ES}A_E, \tag{8b}$$

$$A_A = A_B = A_C = A_D = A_E = A_S, \tag{8c}$$

$$F_{Bi}A_B = F_{Si}A_i = A_iF_{iS}, F_{Ai}A_A = A_iF_{iA}, \tag{8d}$$

$$F_{9E} = F_{9S}(\text{and similar relations}). \tag{8e}$$

Upon substituting (8) into (7), the radiative heat flux $q_{r,Y}$ across surface S in the positive Y-direction can be formulated as:

$$\begin{aligned} q_{r,Y} = \frac{Q_{r,Y}}{A_S} &= \frac{4(A_5F_{5S} + A_9F_{9S})}{A_B}\varepsilon\sigma T^4 + J_BF_{BS} + 4J_AF_{AS} \\ &+ \frac{4(A_5F_{5S}J_B + 2A_5F_{5D}J_A)}{A_B}\rho F_{5S} \\ &+ \frac{4J_AA_9(2F_{9D} + F_{9S})}{A_B}\rho F_{9S} \\ &+ \frac{4(11A_5F_{57}(F_{5S} + F_{9S}))}{A_B}\rho\varepsilon\sigma T^4. \end{aligned} \tag{9}$$

The first line in Eq. (9) is the radiative heat flux due to emission, and the second and third lines are the radiation contributions due to reflectance. Eq. (9) can be further arranged as:

$$q_{r,Y} = \beta_1\varepsilon\sigma T^4 + \beta_2J_B + \beta_3J_A, \tag{10a}$$

where the nondimensional coefficients β_1, β_2 and β_3 are given by:

$$\beta_1 = [4(A_5F_{5S} + A_9F_{9S}) + 44A_5F_{57}(F_{5S} + F_{9S})\rho]/A_B, \tag{10b}$$

$$\beta_2 = F_{BS} + 4A_5F_{5S}^2\rho/A_B, \tag{10c}$$

$$\beta_3 = 4F_{AS} + 4A_5(2F_{5D}F_{5S} + (2F_{9D} + F_{9S})F_{9S})\rho/A_B. \tag{10d}$$

In order to know $q_{r,Y}$, the irradiations on surface B, J_B, and on surface A, J_A, need to be solved. From the above analysis, it is known that J_B is the same as $q_{r,Y}$ in the $(I-1)$th unit cell, given by:

$$J_B = \beta_1\varepsilon\sigma(T + \Delta T)^4 + \beta_2J_B^{(1)} + \beta_3J_A^{(1)}, \tag{11}$$

where $J_B^{(1)}$ and $J_A^{(1)}$ are the corresponding quantities in the $(I-2)$th cell and are determined in Appendix A. Similarly, as shown in Appendix A, the quantity J_A can be expressed in terms of J_B as:

$$J_A = \alpha_1\varepsilon\sigma T^4 + \alpha_2J_B, \tag{12a}$$

where the dimensionless coefficients α_1 and α_2 are given by:

$$\alpha_1 = \frac{2(A_5F_{5D} + A_9F_{9D}) + A_{12}F_{12D} + 11A_5F_{57}(2F_{5D} + 3F_{9D})\rho}{A_A(1 - F_{AD} - 2F_{CD} - A_5/A_A\cdot(4F_{5D}^2 + 9F_{9D}^2)\rho)}, \tag{12b}$$

$$\alpha_2 = \frac{A_AF_{BD} + 2A_5F_{5S}F_{5D}\rho}{A_A[1 - F_{AD} - 2F_{CD} - A_5/A_A\cdot(4F_{5D}^2 + 9F_{9D}^2)\rho]}. \tag{12c}$$

In view of (12), Eq. (10) can be re-written as:

$$q_{r,Y} = (\beta_1 + \beta_3\alpha_1)\varepsilon\sigma T^4 + (\beta_2 + \beta_3\alpha_2)J_B. \tag{13a}$$

Similarly, as illustrated in Appendix B, the radiation heat flux $q_{r,-Y}$ is determined as:

$$q_{r,-Y} = (\beta_1 + \beta_3\alpha_1)\varepsilon\sigma(T - \Delta T)^4 + (\beta_2 + \beta_3\alpha_2)J_{B,-Y}. \tag{13b}$$

Upon substitution of (13) into (6), the net radiation heat flux $q_{r,net}$ becomes:

$$\begin{aligned} q_{r,net} = (\beta_1 + \beta_3\alpha_1)\varepsilon\sigma\{T^4 - (T - \Delta T)^4\} + (\beta_2 + \beta_3\alpha_2) \\ \times (J_B - J_{B,-Y}), \end{aligned} \tag{14}$$

from which the equivalent radiative conductivity is determined as:

$$k_r = \frac{q_{r,net}}{(T_h - T_c)/H}. \tag{15}$$

4. Configuration factors

It is noted again that only a quarter of the solid strut surface is included in a unit cell, with the rest belonging to the neighboring cells. Due to symmetry, the following relations exist:

$$F_{5S} = F_{5B} = F_{9D}, \quad F_{5D} = F_{9S} = F_{12D}, \tag{16a}$$

$$F_{AS} = F_{BD}, \quad F_{AD} = F_{BS}. \tag{16b}$$

In order to determine F_{5S} and F_{5D}, configuration factors $F_{5S'}$ and $F_{5D'}$ are introduced, with the prime in the subscript indicating the surface including the cross-sectional area of the solid struts, e.g., $A_{S'} = A_S + \pi d^2/4$ where $A_{S'}$ and A_S represent the area of surface S with and without the inclusion of the solid part, respectively. A_D and $A_{D'}$ are similarly defined.

The analysis of the configuration factor yields,

$$2F_{5S'} + F_{5E'} + F_{5D'} = 1, F_{5E'} = F_{5D'}, \tag{17a}$$

and

$$F_{5S'} = \frac{1 - 2F_{5D'}}{2}. \tag{17b}$$

For simplicity, F_{5S} and F_{5D} can be written as:

$$F_{5S} = F_{5S'}\frac{A_S}{A_{S'}} \quad \text{and} \quad F_{5D} = F_{5D'}\frac{A_D}{A_{D'}}. \tag{18}$$

The remaining task is to solve the four unknown configuration factors: $F_{5D'}$, F_{AS}, F_{AD} and F_{57}. For illustration, the configuration factor $F_{5D'}$ is calculated below.

The configuration factor between a plane surface I of length c and width b and the surface of a full cylinder II located a distance away from I (Fig. 5) is given by [32,33]:

$$F_{I,II} = \frac{2}{Y_1}\int_0^{Y_1/2} f(\zeta)d\zeta, \tag{19}$$

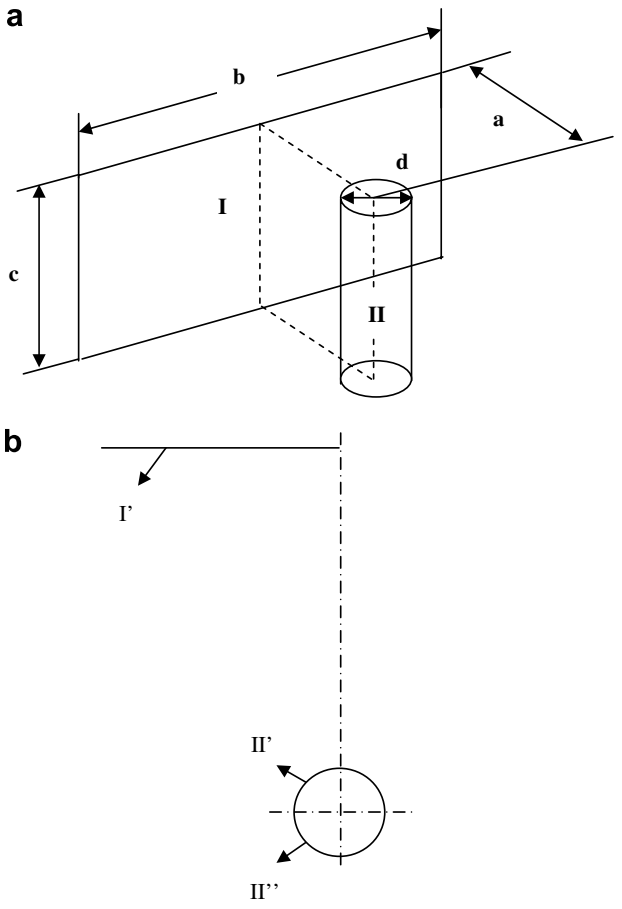

Fig. 5. Configuration factor between a cylinder and a finite plane.

where

$$f(\zeta)=\frac{X_1}{X_1^2+\zeta^2}-\frac{X_1}{\pi(X_1^2+\zeta^2)}\left\{\cos^{-1}\frac{\eta_2}{\eta_1}-\frac{1}{2Z_1}\left[\sqrt{\eta_1^2+4Z_1^2}\cos^{-1}\left(\frac{\eta_2}{\eta_1\sqrt{X_1^2+\zeta^2}}\right)+\eta_2\sin^{-1}\left(\frac{1}{\sqrt{X_1^2+\zeta^2}}\right)-\frac{\pi\eta_1}{2}\right]\right\}, \tag{20a}$$

with

$$X_1=2a/d,\quad Y_1=2b/d,\quad Z_1=2c/d, \tag{20b}$$

$$\eta_1=X_1^2+Z_1^2+\zeta^2-1,\quad \eta_2=Z_1^2-X_1^2-\zeta^2+1. \tag{20c}$$

From the reciprocity relation,

$$A_{\mathrm{I}}F_{\mathrm{I,II}}=A_{\mathrm{II}}F_{\mathrm{II,I}}, \tag{21}$$

the configuration factor from cylinder surface II to plane I, $F_{\mathrm{II,I}}$, can be obtained as:

$$F_{\mathrm{II,I}}=\frac{b}{\pi d}F_{\mathrm{I,II}}. \tag{22}$$

Since both the cylinder and the plane are symmetrical, the configuration factor $F_{\mathrm{II,I}}$ is identical to $F_{\mathrm{II'+II'',I'}}$, as shown in Fig. 5b:

$$F_{\mathrm{II,I}}=F_{\mathrm{II'+II'',I'}}, \tag{23}$$

where I′ is half of plane I, and II′ and II″ are both a quarter of the full cylinder surface.

For the case studied, the configuration factor $F_{5D'}$ corresponds to that from II″ to I′, so $F_{\mathrm{II',I'}}$ is needed. Based on the physical definition of the configuration factor and by noting that the energy emitted from surface II″ cannot reach surface I′, the value of $F_{\mathrm{II',I'}}$ is twice that of $F_{\mathrm{II'+II'',I'}}$, namely:

$$F_{\mathrm{II',I'}}=2F_{\mathrm{II'+II'',I'}}=2F_{\mathrm{II},I}=\frac{2b}{\pi d}F_{\mathrm{I,II}}. \tag{24}$$

Then, $F_{5D'}$ can be obtained as long as the same dimensions in Fig. 4 are used, as:

$$F_{5D'}=F_{\mathrm{II',I'}}. \tag{25}$$

After $F_{5D'}$ is known, the configuration factors, F_{5D}, F_{5S}, F_{5B}, F_{9S}, F_{9D} and F_{12D}, can be obtained from Eqs. (16), (17) and (18).

The calculation of F_{AS} and F_{AD} is more straightforward, and the following cross-relationship holds:

$$4F_{AS}+F_{AD}=1. \tag{26}$$

The formulations of F_{AS}, F_{AD} and F_{57} can be found in [29,30], and hence will not be repeated here.

5. Results and discussion

To demonstrate the predictive capability of the model, a FeCrAlY foam sample with 60 ppi and 5% relative density having the same physical dimensions and boundary conditions as the test sample [30] is considered. From Eqs. (13a), (A.5), (A.6), (B.5) and (B.6), it is seen that the analytical solution depends on the irradiation series of $J_B, J_B^{(1)}, J_B^{(2)},\ldots,J_B^{(M+1)}$ and $J_{B,-Y}, J_{B,-Y}^{(1)}, J_{B,-Y}^{(2)},\ldots,J_{B,-Y}^{(N_{\mathrm{cell}}-M+1)}$. Here, the model is said to have first-order accuracy if only $(J_B, J_B^{(1)})$ and $(J_{B,-Y}, J_{B,-Y}^{(1)})$ are reserved, with terms $(J_B^{(2)},\ldots,J_B^{(M+1)})$ and $(J_{B,-Y}^{(2)},\ldots,J_{B,-Y}^{(N_{\mathrm{cell}}-M+1)})$ neglected. Physically, the first-order accuracy implies that the calculated radiation for one unit cell only accounts for the contribution from the immediately adjacent neighboring cells. Similarly, for second-order accuracy, the model keeps the J_B and $J_{B,-Y}$ series up to $J_B^{(2)}$ and $J_{B,-Y}^{(2)}$, i.e., the two-layer neighboring cells are included in the calculation. Fig. 6 compares the analytically predicted radiative conductivity k_{r} with test data taken from [30] for the temperature range of 300–800 K. To extract the net radiative contribution from the total conductivity measured in vacuum, the analytical model of solid conduction [8] has been used. Fig. 6 reveals that the analysis based only on the neighboring cells is not accurate, as the predicted k_{r} based on the first-order accuracy model has a value less than half of the full analytical solution, but the predictions based on the sixth-order

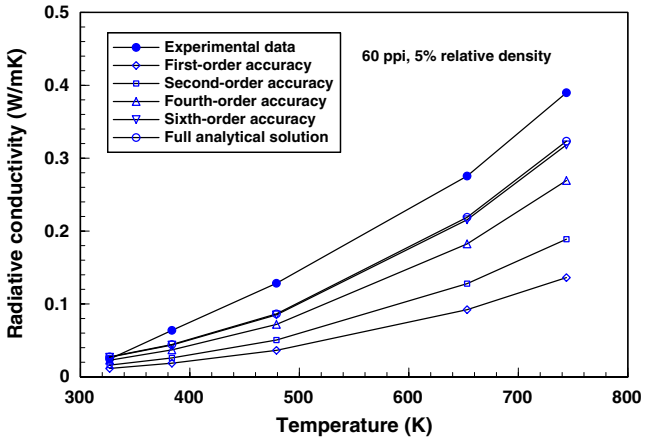

Fig. 6. Predicted effective radiative conductivity plotted as a function of temperature for FeCrAlY foam with 60 ppi and 5% relative density; experimental data from [30] are included for comparison.

accuracy are very close to the full analytical solution (Fig. 6).

For the other four foam samples with different cell sizes and relative densities that are tested in [30], the results are shown in Figs. 7–10 together with model predictions. These results show that the analytical solution predicts the correct trend of the experimental curve, although the predictions are about 10–20% less than those measured. Given the complexity of the thermal radiation process and the various assumptions made to simplify the analysis (e.g., idealized foam structure, linear temperature variation, spectrally independent radiation properties, and uncertainty of the solid material emissivity, ε), the accuracy of the present analytical model is considered reasonable.

5.1. Reflectance effect

The present analysis based on a model structure shows that both the solid emission and reflectance contribute to the radiative conductivity. The predicted radiative conductivity with and without the effect of reflectance is shown in Fig. 11, and it can be seen that the contribution of reflec-

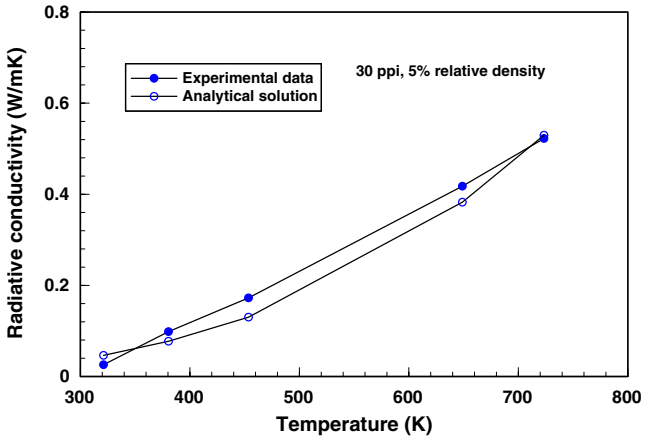

Fig. 7. Predicted effective radiative conductivity plotted as a function of temperature for FeCrAlY foam with 30 ppi and 5% relative density; experimental data from [30] are included for comparison.

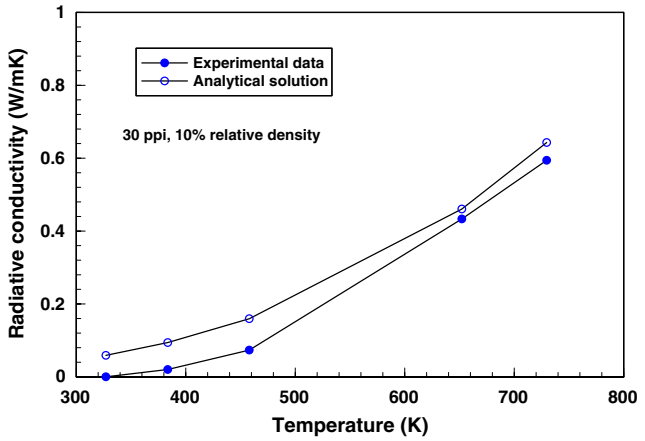

Fig. 8. Predicted effective radiative conductivity plotted as a function of temperature for FeCrAlY foam with 30 ppi and 10% relative density; experimental data from [30] are included for comparison.

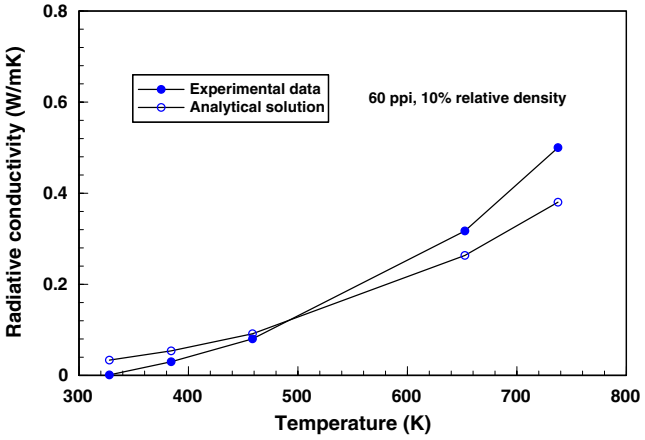

Fig. 9. Predicted effective radiative conductivity plotted as a function of temperature for FeCrAlY foam with 60 ppi and 10% relative density; experimental data from [30] are included for comparison.

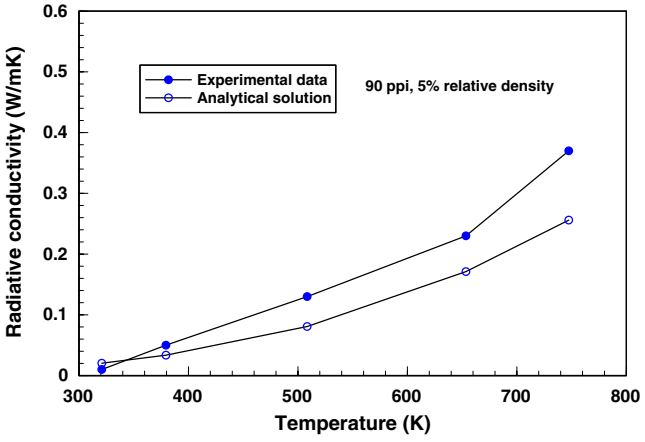

Fig. 10. Predicted effective radiative conductivity plotted as a function of temperature for FeCrAlY foam with 90 ppi and 5% relative density; experimental data from [30] are included for comparison.

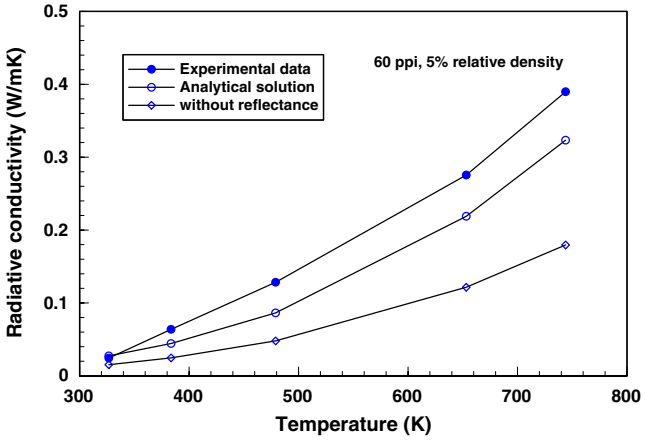

Fig. 11. Effect of reflectance on thermal radiation for FeCrAlY foam with 60 ppi and 5% relative density.

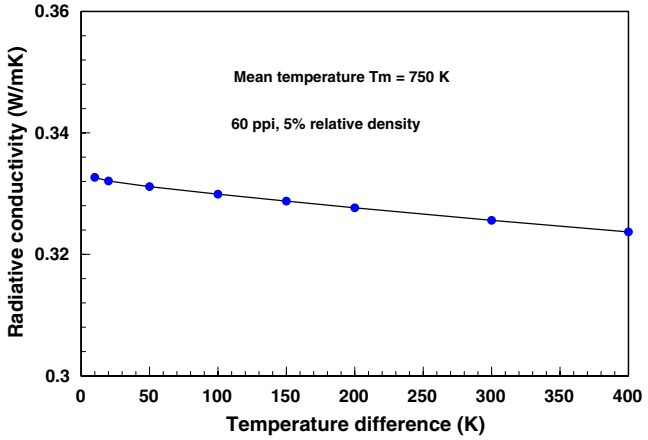

Fig. 13. Effect of temperature gradient on radiative conductivity of FeCrAlY foam with 60 ppi and 5% relative density.

tance is very significant, accounting for approximately 40% of the total radiative conductivity.

5.2. Influence of solid emissivity

It is known that the emissivity of a solid material varies significantly, and it is dependent upon surface situations (e.g., roughness) and temperature. Generally, the emissivity of steel varies between 0.3 and 0.8 [16]. Fig. 12 shows the effect of solid emissivity on the predicted radiative heat transfer at a given temperature $T = 750$ K. It is seen that the variation of solid emissivity between 0.3 and 0.8 has negligible effect on the predicted results. Even though a larger emissivity can lead to higher emitting radiation, the reflectance contribution will become smaller. The combined effect of emission and reflectance contributions determines the overall effect on the radiative heat transfer.

5.3. Temperature gradient effect

To measure the effective thermal conductivity experimentally, a temperature gradient must be imposed on the foam sample, and the effective conductivity obtained is expressed in terms of the mean sample temperature [30]. The sensitivity of the predicted radiative conductivity to variations in the imposed temperature difference ΔT between the top and bottom surfaces of the foam sample of fixed thickness 25 mm and mean sample temperature $T_m = 750$ K is shown in Fig. 13.

It can be seen from Fig. 13 that the temperature gradient effect is small for the temperature range studied: less than 5% between $\Delta T = 10$ K and $\Delta T = 400$ K. For the experimental data obtained in [30], the maximum temperature difference imposed is about 50 K, so the uncertainty due to temperature gradient is less than 2%, as shown in Fig. 13.

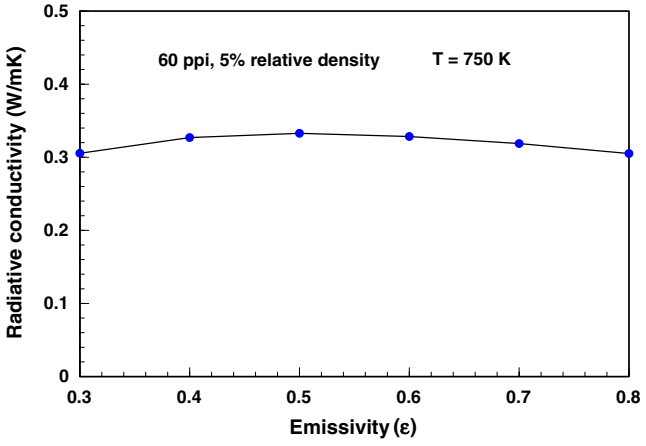

Fig. 12. Influence of solid emissivity on radiative conductivity for FeCrAlY foam with 60 ppi and 5% relative density.

5.4. Strut shape effect

In the analysis thus far the cell struts of the model metal foam have been modeled as circular cylinders, although the cross-sectional shape of the cell strut of a real metal foam is irregular. Throughout the analysis, the effect of different strut shapes is only brought in by the configuration factors and the strut surface area. Statistically, the configuration factors between the solid struts and the void surfaces within a unit cell should be essentially identical as long as the porosity remains unchanged and high (>90%).

Consequently, only the effect of strut surface areas for different strut shapes will be considered. Here, a triangular cross-sectional shape is assumed based on the same cross-sectional area of the circular cylindrical strut, as shown in Fig. 14. The calculations are shown in Fig. 15 for the foam sample with 60 ppi and 5% relative density. It can be seen that the strut shape effect on the thermal radiation is small. This can be attributed to the large porosity of the metal foam (>90%), so the porosity and the practical foam structure should have more significant effects. This observation is important, as it proves the validity of the previous effective medium approach based on the diffusion approximation utilizing the Rosseland mean coefficient [31], where the effect of strut shape is neglected.

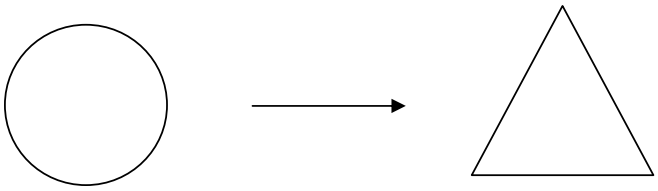

Fig. 14. Cylindrical solid strut versus triangular solid strut.

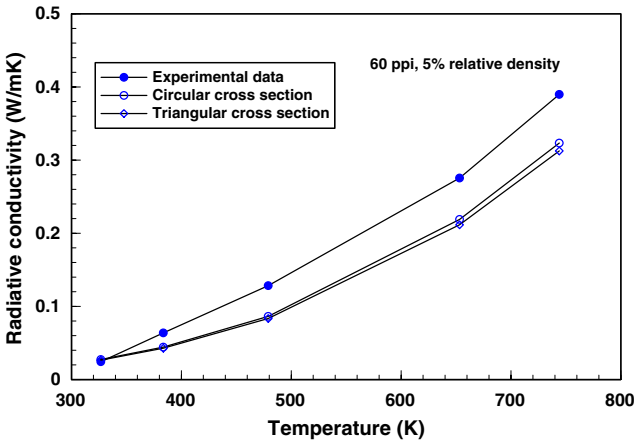

Fig. 15. Effect of solid strut cross-sectional shape on radiative conductivity of FeCrAlY foam with 60 ppi and 5% relative density.

5.5. Effect of basic foam parameters

Three independent parameters characterizing a cellular metal foam have been identified in previous studies [10,11], namely, relative density (ρ_r), pore size (d'_p), and ligament diameter (d). The cross relationship amongst the three parameters can be written as [10,11]:

$$\frac{d}{d'_p} = 1.18\sqrt{\frac{1-\phi}{3\pi}}\left(\frac{1}{1-e^{-((1-\phi)/0.04)}}\right), \quad (27)$$

where $\phi(=1-\rho_r)$ is the porosity.

The predicted effect of cell size on the radiative conductivity of a foam with a fixed average temperature of 750 K and a fixed relative density of 5% is shown in Fig. 16. It is seen that the radiative conductivity increases linearly with increasing cell size. As the cell size increases, from Eq. (27) it is known that the solid strut diameter, d, also increases in order to maintain the same relative density. This implies that more radiation will be emitted and reflected by the solid strut surfaces, and hence a bigger cell size leads to a larger "penetration thickness". Larger "penetration thickness" means that more heat can be directly transferred by thermal radiation to a deeper thickness of the foam before it decays to a lower level. This process greatly reduces the total thermal resistance and results in a higher effective radiative conductivity, as exhibited in Fig. 16. The same conclusion has been reached in the measurements [30].

Fig. 17 presents the effect of foam relative density on the radiative conductivity for a fixed cell size (1 mm) and a

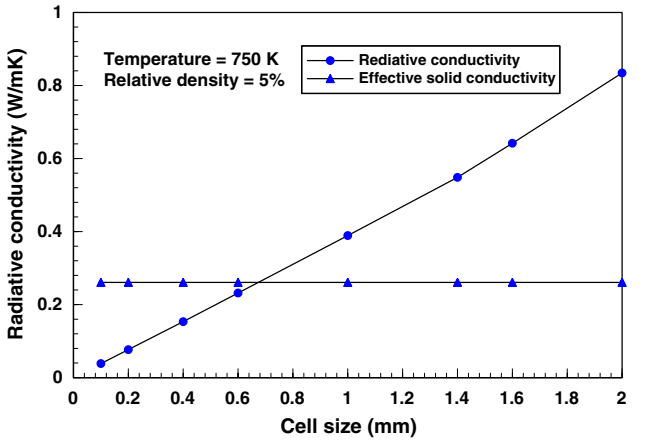

Fig. 16. Effect of cell size on radiative conductivity of FeCrAlY foam with 60 ppi and 5% relative density.

fixed average foam temperature of 750 K. It is seen that the radiative conductivity increases with increasing relative density, reaching gradually a plateau. At a given cell size, a larger relative density leads to a larger strut diameter according to (27). More radiation will therefore be emitted by the solid strut surfaces, but more solid strut surfaces at a given cell size will obstruct the thermal radiation transferred to a deeper foam thickness. In other words, the "penetration thickness" becomes smaller or, equivalently, the extinction coefficient becomes larger. The combined effects dictate the trend shown in Fig. 17.

From the well-established effective solid conductivity model [8], the effect of foam parameters on effective solid conductivity can be obtained, and the results are shown in Figs. 16 and 17 together with the radiative conductivity. For a fixed relative density, the effective solid conductivity is independent of the cell size, whereas it linearly increases with the relative density at a given cell size.

From Figs. 16 and 17, it is seen that the total effective thermal conductivity (sum of effective solid conductivity and radiative conductivity) of a metal foam increases with increasing cell size and increasing relative density.

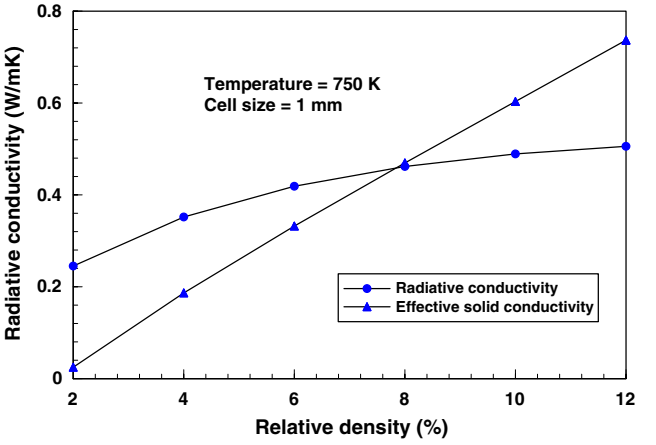

Fig. 17. Effect of relative density on radiative conductivity of FeCrAlY foam with 5% relative density and average temperature of 750 K.

6. Conclusions

An explicit analytical model is developed to describe the thermal radiation process in open-celled metal foams with idealized cellular morphologies. The results show that the contribution of reflectance to radiation can be as high as 50% and hence cannot be neglected. The radiative conductivity increases linearly with increasing cell size for a fixed relative density, but for a given cell size increasing the relative density has a relatively small effect on the radiative conductivity due to the combined effect of increased emission and extinction. There is a slight drop in the radiative conductivity when the temperature gradient imposed on the foam sample is increased (but with the average foam temperature kept unchanged). The model predicts the correct trend of the experimentally measured conductivity versus temperature curve for steel alloy foams, although the predicted conductivity is in general 10–20% below that measured. This has been attributed to the various assumptions introduced to simplify the analysis, e.g., cubit unit cell, spectrally independent radiation properties, and uncertainty of the solid material emissivity.

Acknowledgements

This work is supported partly by the UK Engineering and Physical Science Research Council (EPSRC Grant No. GR/T24364/01), National Natural Science Foundation of China (No. 50576069), National Basic Research Programme of China (No. 2006CB601203) and the program for New Century Excellent Talents in University (NCET-04-0944). We would like to thank Mr. Ian Stirling and Mr. Ken Butcher of Porvair Fuel Cell Technology for providing the FeCrAlY foam samples, and Prof. J.D. Jackson and Dr. Z. Xu of University of Manchester for experimental assistance.

Appendix A

Eq. (10) gives the irradiation on surface B, J_B, which is also the $q_{r,Y}$ in the $(I-1)$th unit cell. Similarly,

$$J_B^{(1)} = \beta_1\varepsilon\sigma(T+2\Delta T)^4 + \beta_2 J_B^{(2)} + \beta_3 J_A^{(2)}, \tag{A.1a}$$

$$J_B^{(2)} = \beta_1\varepsilon\sigma(T+3\Delta T)^4 + \beta_2 J_B^{(3)} + \beta_3 J_A^{(3)}, \tag{A.1b}$$

$$\cdots$$

$$J_B^{(M)} = \beta_1\varepsilon\sigma(T+(M+1)\Delta T)^4 + \beta_2 J_B^{(M+1)} + \beta_3 J_A^{(M+1)}, \tag{A.1m}$$

where $J_B^{(M+1)}$ is the emitting radiation from the bottom boundary of the foam sample having temperature T_h, given by:

$$J_B^{M+1} = \varepsilon\sigma T_h^4. \tag{A.2}$$

Since $J_A, J_A^{(1)}, \ldots, J_A^{(M+1)}$ appear in the above series of equations, their formulations need to be specified, as illustrated below.

By symmetry, the irradiation on the side surface A, J_A, is identical to the irradiation on the side surfaces C, D, and E, i.e., $J_A = J_C = J_D = J_E$. The formulation of J_A for the Ith unit cell is similar to that for J_B given in Eq. (8), with:

$$\begin{aligned} J_A = {} & \frac{[2(A_5F_{5D}+A_9F_{9D})+A_{12}F_{12D}]}{A_A}\varepsilon\sigma T^4 + J_A F_{AD} \\ & + J_C F_{CD} + J_E F_{ED} + J_B F_{BD} \\ & + \frac{2(A_5F_{5S}J_B + 2A_5F_{5D}J_A)}{A_A}\rho F_{5D} \\ & + \frac{3(3A_9F_{9D}J_A)}{A_A}\rho F_{9D} \\ & + \frac{11A_5F_{57}(2F_{5D}+3F_{9D})}{A_A}\rho\varepsilon\sigma T^4, \end{aligned} \tag{A.3}$$

where F_{5D}, F_{9D} and F_{12D} are the configuration factors from strut surfaces 5, 9 and 12 to side surface D, F_{AD}, F_{CD} and F_{ED} are the configuration factors from side surfaces A, C and E to surface D, and F_{BD} is the configuration factor from surface B to surface D. The first line in (A.3) represents emission, whereas the second and third lines are the contributions from reflectance.

The relationship between J_A and J_B for the Ith unit cell is built via Eq. (12a). Similarly, the following series of equations can be obtained for all unit cells beneath the Ith cell:

$$J_A^{(1)} = \alpha_1\varepsilon\sigma(T+\Delta T)^4 + \alpha_2 J_B^{(1)}, \tag{A.4a}$$

$$J_A^{(2)} = \alpha_1\varepsilon\sigma(T+2\Delta T)^4 + \alpha_2 J_B^{(2)}, \tag{A.4b}$$

$$\cdots$$

$$J_A^{(M+1)} = \alpha_1\varepsilon\sigma(T+(M+1)\Delta T)^4 + \alpha_2 J_B^{(M+1)}. \tag{A.4m}$$

Once $J_A, J_A^{(1)}, \ldots, J_A^{(M+1)}$ are known, J_B can be determined by substituting (11) and (A.4) into (10) and (A.1), yielding:

$$J_B = (\beta_1+\beta_3\alpha_1)\varepsilon\sigma(T+\Delta T)^4 + (\beta_2+\beta_3\alpha_2)J_B^{(1)}, \tag{A.5a}$$

$$J_B^{(1)} = (\beta_1+\beta_3\alpha_1)\varepsilon\sigma(T+2\Delta T)^4 + (\beta_2+\beta_3\alpha_2)J_B^{(2)}, \tag{A.6a}$$

$$J_B^{(2)} = (\beta_1+\beta_3\alpha_1)\varepsilon\sigma(T+3\Delta T)^4 + (\beta_2+\beta_3\alpha_2)J_B^{(3)}, \tag{A.6b}$$

$$\cdots$$

$$\begin{aligned} J_B^{(M)} = {} & (\beta_1+\beta_3\alpha_1)\varepsilon\sigma(T+(M+1)\Delta T)^4 \\ & + (\beta_2+\beta_3\alpha_2)J_B^{(M+1)}. \end{aligned} \tag{A.6m}$$

Appendix B

The radiation heat flux in the negative direction on the top void surface B of the Ith unit cell, $J_{B,-Y}$, can be obtained as:

$$J_{B,-Y} = \beta_1\varepsilon\sigma(T-2\Delta T)^4 + \beta_2 J_{B,-Y}^{(1)} + \beta_3 J_{A,-Y}^{(1)}, \tag{B.1}$$

$$J_{B,-Y}^{(1)} = \beta_1\varepsilon\sigma(T-3\Delta T)^4 + \beta_2 J_{B,-Y}^{(2)} + \beta_3 J_{A,-Y}^{(2)}, \tag{B.2a}$$

$$J_{B,-Y}^{(2)} = \beta_1\varepsilon\sigma(T-4\Delta T)^4 + \beta_2 J_{B,-Y}^{(3)} + \beta_3 J_{A,-Y}^{(3)}, \tag{B.2b}$$

$$\cdots$$

$$J_{B,-Y}^{(N)} = \beta_1\varepsilon\sigma(T-(N+2)\Delta T)^4 + \beta_2 J_{B,-Y}^{(N)} + \beta_3 J_{A,-Y}^{(N+1)}, \tag{B.2n}$$

where $N = N_{\text{cell}} - M$. Similarly, by considering the radiation from all unit cells lying above the Ith cell, one obtains:

$$J_{A,-Y} = \alpha_1 \varepsilon\sigma(T - \Delta T)^4 + \alpha_2 J_{B,-Y}, \tag{B.3}$$

$$J^{(1)}_{A,-Y} = \alpha_2 J^{(1)}_{B,-Y} + \alpha_1 \varepsilon\sigma(T - 2\Delta T)^4, \tag{B.4a}$$

$$J^{(2)}_{A,-Y} = \alpha_2 J^{(2)}_{B,-Y} + \alpha_1 \varepsilon\sigma(T - 3\Delta T)^4, \tag{B.4b}$$

$$\cdots$$

$$J^{(N)}_{A,-Y} = \alpha_2 J^{(N)}_{B,-Y} + \alpha_1 \varepsilon\sigma(T - (N+1)\Delta T)^4, \tag{B.4n}$$

where the nondimensional coefficients α_1 and α_2 are found in Eqs. (12b) and (12c).

Finally, substitution of (B.3) and (B.4) into (B.1) and (B.2) yields the following series equations for $J_{B,-Y}$:

$$J_{B,-Y} = (\beta_1 + \beta_3\alpha_1)\varepsilon\sigma(T - 2\Delta T)^4 + (\beta_2 + \beta_3\alpha_2)J^{(1)}_{B,-Y}, \tag{B.5}$$

$$J^{(1)}_{B,-Y} = (\beta_1 + \beta_3\alpha_1)\varepsilon\sigma(T - 3\Delta T)^4 + (\beta_2 + \beta_3\alpha_2)J^{(2)}_{B,-Y}, \tag{B.6a}$$

$$J^{(2)}_{B,-Y} = (\beta_1 + \beta_3\alpha_1)\varepsilon\sigma(T - 4\Delta T)^4 + (\beta_2 + \beta_3\alpha_2)J^{(3)}_{B,-Y}, \tag{B.6b}$$

$$\cdots$$

$$J^{(N)}_{B,-Y} = (\beta_1 + \beta_3\alpha_1)\varepsilon\sigma(T - (N+1)\Delta T)^4 + (\beta_2 + \beta_3\alpha_2)J^{(N+1)}_{B,-Y}, \tag{B.6n}$$

where $J^{(N+1)}_{B,-Y}$ is the radiation heat flux emitted from the upper boundary of the foam sample with temperature T_c:

$$J^{(N+1)}_{B,-Y} = \varepsilon\sigma T_c^4, \tag{B.7}$$

References

[1] T.J. Lu, H.A. Stone, M.F. Ashby, Heat transfer in open-celled metal foams, Acta Mater. 46 (1998) 3619–3635.

[2] A.G. Evans, J.W. Hutchinson, M.F. Ashby, Multifunctionality of cellular metal systems, Prog. Mater. Sci. 43 (1999) 171–221.

[3] T.J. Lu, C. Chen, Thermal transport and fire retardance properties of cellular aluminium alloys, Acta Mater. 47 (1999) 1469–1485.

[4] S. Gu, T.J. Lu, A.G. Evans, On the design of two-dimensional cellular metals for combined heat dissipation and structural load capacity, Int. J. Heat Mass Transfer 44 (2001) 2163–2175.

[5] V.V. Calmidi, R.L. Mahajan, The effective thermal conductivity of high porosity fibrous metal foams, ASME J. Heat Transfer 121 (1999) 466–471.

[6] V.V. Calmidi, R.L. Mahajan, Forced convection in high porosity metal foams, ASME J. Heat Transfer 122 (2000) 557–565.

[7] J.W. Paek, B.H. Kang, S.Y. Kim, J.M. Hyun, Effective thermal conductivity and permeability of aluminium foam materials, Int. J. Thermophys. 21 (2000) 453–464.

[8] K. Boomsma, D. Poulikakos, On the effective thermal conductivity of a three-dimensionally structured fluid-saturated metal foam, Int. J. Heat Mass Transfer 44 (2001) 827–836.

[9] K. Boomsma, D. Poulikakos, The effects of compression and pore size variations on the liquid flow characteristics in metal foams, Trans. ASME J. Fluid Eng. 124 (2002) 263–272.

[10] C.Y. Zhao, T. Kim, T.J. Lu, H.P. Hodson, Modeling on thermal transport in cellular metal foams, in: 8thJoint AIAA/ASME Thermophysics and Heat Transfer Conference, AIAA 2002-3014, St. Louis, MO, USA, June 2002.

[11] C.Y. Zhao, T. Kim, T.J. Lu, H.P. Hodson, Thermal transport in high porosity cellular metal foams, AIAA J. Thermophys. Heat Transfer 18 (3) (2004) 309–317.

[12] T.J. Lu, A. Hess, M.F. Ashby, Sound absorption in metallic foams, J. Appl. Phys. 85 (1999) 7528–7539.

[13] T.J. Lu, F. Chen, D.P. He, Sound absorption of cellular metals with semi-open cells, J. Acoust. Soc. Am. 108 (2000) 1697–1709.

[14] T. Kim, A.J. Fuller, H.P. Hodson, T.J. Lu, An experimental study on thermal transport in lightweight metal foams at high Reynolds numbers, in: Proceedings of the International Symposium of Compact Heat Exchangers, Grenoble, France, 2002, pp. 227–232.

[15] D. Haack, K. Butcher, T. Kim, H.P. Hodson, T.J. Lu, Novel lightweight metal foam heat exchanger, in: ASME International Mechanical Engineering Congress & Exposition, Proceedings V.3 (PID-4B: Heat Exchangers Applications for Change of Phase Media and Fuel Cells Systems, Book No. I00548), 2001, New York.

[16] M.L. Hunt, C.L. Tien, Effects of thermal dispersion on forced convection in fibrous media, Int. J. Heat Mass Transfer 31 (1988) 301–309.

[17] L.B. Younis, R. Viskanta, Experimental determination of the volumetric heat transfer coefficient between stream of air and ceramic foam, Int. J. Heat Mass Transfer 36 (1993) 1425–1434.

[18] Y.C. Lee, W. Zhang, H. Xie, R.L. Mahajan, 1993, Cooling of a FCHIP package with 100 w, 1 cm^2 chip, in: Proceedings of the 1993 ASME International Electronics Packaging Conference, vol. 1, ASME, New York, pp. 419–423.

[19] S.Y. Kim, J.W. Paek, B.H. Kang, Flow and heat transfer correlations for porous fin in a plate-fin heat exchanger, ASME J. Heat Transfer 122 (2000) 572–578.

[20] C.Y. Zhao, T.J. Lu, H.P. Hodson, Natural convection in metal foams with open cells, Int. J. Heat Mass Transfer 48 (2005) 2452–2463.

[21] W. Lu, C.Y. Zhao, S.A. Tassou, Thermal analysis on metal-foam filled heat exchangers, Part I: metal-foam filled tubes, Int. J. Heat Mass Transfer 49 (2006) 2751–2761.

[22] C.Y. Zhao, W. Lu, S.A. Tassou, Thermal analysis on metal-foam filled heat exchangers, Part II: tube heat exchangers, Int. J. Heat Mass Transfer 49 (2006) 2762–2770.

[23] N. Dukhan, K.C. Chen, Heat transfer measurements in metal foam subjected to constant heat flux, Exp. Therm. Fluid Sci. 32 (2) (2007) 624–631.

[24] F. Laurencelle, J. Goyette, Simulation of heat transfer in a metal hydride reactor with aluminium foam, Int. J. Hydrogen Energy 32 (2007) 957–2964.

[25] W. Azzi, W.L. Roberts, A. Rabiei, A study on pressure drop and heat transfer in open cell metal foams for jet engine applications, Mater. Des. 28 (2007) 569–574.

[26] K.C. Leong, L.W. Jin, Effect of oscillatory frequency on heat transfer in metal foam heat sinks of various pore densities, Int. J. Heat Mass Transfer 49 (2006) 671–681.

[27] N. Dukhan, P.D. Quinones-Ramos, E. Cruz-Ruiz, One-dimensional heat transfer analysis in open cell 10 ppi metal foam, Int. J. Heat Mass Transfer 48 (2005) 5112–5120.

[28] S.B. Sathe, R.E. Peck, T.W. Tong, A numerical analysis of heat transfer and combustion in porous radiant burners, Int. J. Heat Mass Transfer 33 (6) (1990) 1331–1338.

[29] T.W. Tong, S.B. Sathe, R.E. Peck, Improving the performance of porous radiant burners through use of sub-micron size fibers, Int. J. Heat Mass Transfer 33 (6) (1990) 1339–1346.

[30] C.Y. Zhao, T.J. Lu, H.P. Hodson, J.D. Jackson, The temperature dependence of effective thermal conductivity of open-celled steel alloy foams, Mater. Sci. Eng.: A 367 (2004) 123–131.

[31] C.Y. Zhao, T.J. Lu, H.P. Hodson, Thermal radiation in metal foams with open cells, Int. J. Heat Mass Transfer 47 (2004) 2927–2939.

[32] R. Siegel, J.R. Howell, Thermal Radiative Heat Transfer, third ed., Hemisphere Publishing, Washington, DC, 1992.

[33] E.M. Sparrow, R.D. Cess, Radiation Heat Transfer, Hemisphere Publishing Corp., Washington, DC, 1978.